International Journal of Impact Engineering 60 (2013) 67–75

Contents lists available at SciVerse ScienceDirect

International Journal of Impact Engineering

journal homepage: www.elsevier.com/locate/ijimpeng

Validation of Johnson-Cook plasticity and damage model using impact experiment

Xuemei Wang*, Jun Shi [1]

United Technologies Research Center, 411 Silver Lane, East Hartford, CT 06108, USA

ARTICLE INFO

Article history:
Received 17 October 2012
Received in revised form
28 February 2013
Accepted 22 April 2013
Available online 2 May 2013

Keywords:
Johnson–Cook
Impact
High strain rate
Foreign object damage

ABSTRACT

The validity of the Johnson–Cook constitutive relation and failure criterion at high strain rates, up to $\sim 10^6\ s^{-1}$, was assessed by predicting the dynamic response of Ti–6Al–4V under high-speed ball impact at various velocities and angles. White-light scanning was performed to characterize impact craters formed on target surfaces. The measured crater was compared with that predicted by the corresponding finite element model developed using the finite element code Abaqus/Explicit. The target material behavior was modeled by the Johnson–Cook material model that induced both plastic deformation and damage mechanism. Good agreement was obtained between the experimental measurements and numerical predictions for all testing conditions.

1. Introduction

Metal deformation and rupture under impact loading is a complex and dynamic process, always involving high plastic strains as well as large changes in strain rates. The Johnson–Cook (J–C) material model has been widely used to model impact and penetration-related problems [1–5]. However, the validity of the J–C material model to simulate the dynamic material behavior and failure under impact loading relevant to the applications, such as sand erosion and foreign object damage (FOD), remains to be confirmed.

Sand erosion results in material loss by repeated impact of small solid particles at high impinging velocities. For example, helicopter rotor blades in a desert environment experience severe sand erosion, resulting in excessive wear damage at the leading edges. Computer modeling provides an effective method complementary to experimental techniques for fundamental understanding of erosion mechanism and for predicting material performance during erosion process [6–10]. Since material erosion is a complex phenomenon, often including high strain/strain-rate deformations and failure/damage processes, it is crucial to use appropriate and validated material constitutive models in order to model erosion process. The work presented in this paper is motivated by this goal. The approach involves experimentation and computational numerical modeling of single impact based on the FOD event.

In contrast to multiple impacts in erosion, the FOD test in a laboratory is designed to perform single particle impact at the velocity range similar to that in erosion conditions, but with better user-controlled conditions on various parameters, such as impact angles and velocities. A full analysis of the problem requires not only a valid form of constitutive relation but also inclusion of a failure criterion defining the limit of plastic deformation. The appropriate constitutive behavior of the material is augmented by damage initiation and damage propagation relationships that allow for complete element failure and removal, thus allowing for explicit simulation of the material removal process.

A survey of the literature shows a variety of constitutive models used for FOD simulations of metallic systems, including J–C, Bammann, and Armstrong-Zerilli material models. Duó et al. [11] experimentally and numerically investigated residual stresses after FOD damage. In their experiments, FOD was introduced by firing a hardened steel cube on the leading edge of a Ti–6Al–4V blade section, and the residual stresses were evaluated using both laboratory low energy monochromatic stress measurement and high-energy white beam synchrotron stress measurement. They compared their experimental results with the finite element model from which the residual stress pattern following simulated impact was calculated using Bammann damage material model.

* Corresponding author. Tel.: +1 860 610 7086; fax: +1 860 353 3201.
E-mail address: wangxm@utrc.utc.com (X. Wang).
[1] Present address: Rolls-Royce Corporation, 2001 South Tibbs Avenue, Indianapolis, IN 46241, USA.

0734-743X/$ – see front matter © 2013 Published by Elsevier Ltd.
http://dx.doi.org/10.1016/j.ijimpeng.2013.04.010

Macdougall and Harding [2] studied Armstrong-Zerilli type constitutive relation and validated it using tensile Hopkinson bar tests at impact rates from 1000 to 3500 s^{-1}. The calibration of the material constants used in the Zerilli–Armstrong relation were performed with use of torsional Hopkinson bar tests at shear strain rates from 7×10^{-4} to 1000 s^{-1}. Reasonable agreement was reported between the experimental results and the numerical predictions. In this paper, the J–C material model was investigated. The calibration of J–C parameters were based on quasi-static tensile tests and Hopkinson bar tests, in which materials are usually tested at strain rates typically ranged from 10^{-3} to 5000 s^{-1} [12,13].

The finite element simulation of FOD events suggests that strain rates are of the order of 10^6 s^{-1} [11], whereas it is difficult in practice to obtain material data at strain rate greater than 10^3 s^{-1}. Hence it is almost inevitable to extrapolate material behavior into the very high strain rate regime. Therefore, for the purposes of numerical model validation, it is essential to ensure that the material model used is suitable to predict the real impact damage and deformation.

In the present work, experimental measurement of post-impact deformation was compared against numerical prediction based on the simulated impact model developed using the finite element analysis package Abaqus (SIMULIA, 2010). One particular challenge for numerical simulation is the fact that strain rates of the order of 10^6 s^{-1} may be experienced during the impact, which are significantly higher than the typical rates at which material properties are measured. The validity of both the constitutive relation and the failure criterion (in the present work, the J–C plasticity and damage model) was assessed in terms of its ability to predict FOD-induced deformation and damage observed in the experiments. Such validation of the material models can provide the confidence in using them in modeling complex erosion process that involves higher strain rates as well.

2. Experimental details

2.1. Materials

The target material studied in this investigation was titanium alloy Ti–6Al–4V. The specimens were machined from as-received plates (thickness of 3.175 mm) into specimen with the dimension of 25.4 mm × 25.4 mm. Two projectile materials were chosen in this work: dense high-alumina ceramic (99.5–99.8% Al_2O_3) and high strength steel (McMaster-Carr, GA). All projectiles were spherical in shape with a diameter of 6.35 mm. The basic mechanical properties of Ti–6Al–4V as well as of the projectile materials are summarized in Table 1.

2.2. Experimental procedure

FOD tests were conducted at ambient temperature using a gas-gun apparatus available at the United Technologies Research Center (UTRC). The FOD test method is capable of introducing deformation and damage in the Ti–6Al–4V substrate that is representative of the real impact conditions such as high strain rate effects on material deformation. Fig. 1a shows a schematic of the FOD test

Table 1
Basic mechanical properties of target and projectile materials.

Material properties	Symbol	Alumina	Steel	Ti–6Al–4V
Density	ρ (kg/m^3)	3902.5	7971	4428
Young's modulus	E (GPa)	300	203.6	109.8
Poisson's ratio	ν	0.21	0.3	0.31
Yield stress	σ_y (MPa)	–	2340	1098

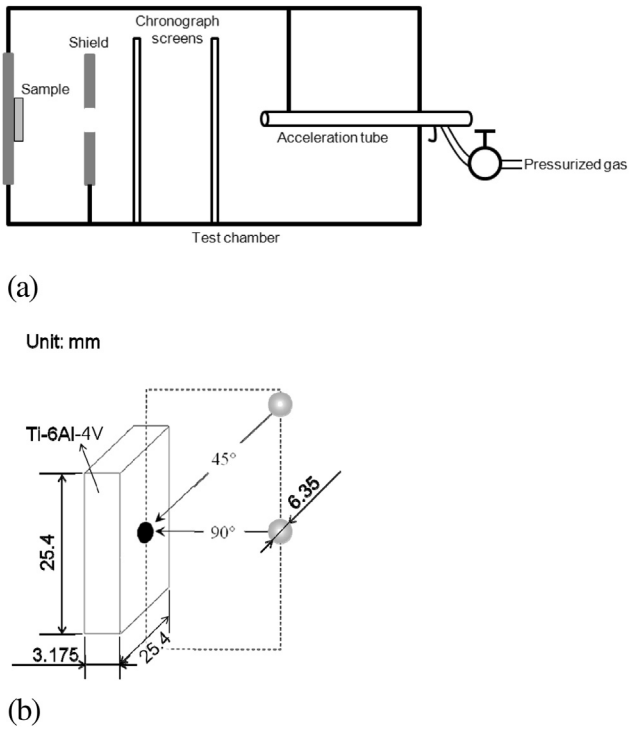

Fig. 1. Schematic of (a) FOD testing rig and (b) impact angles with respect to specimen geometry: In this study, a normal (90°) and an oblique (45°) impact considered.

utilized. During the test, the projectile was inserted into an acceleration tube until stop. A helium-gas cylinder and pressurize accumulator were used to pressurize the reservoir to a specific level, depending on prescribed impact velocity. Upon reaching a specific level of pressure, a solenoid valve was instantaneously opened accelerating the projectile through the acceleration tube to impact on the target specimen. The target specimen was fully supported using a rigid steel block. The target specimen was aligned such that the projectile impacted on its flat surface at

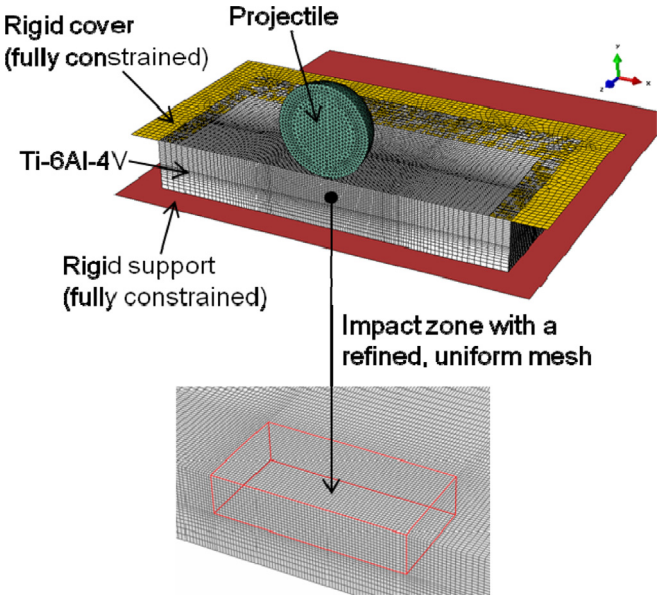

Fig. 2. FE model of the FOD test.

Table 2
Material parameters for Ti–6Al–4V.

Material properties	Symbol	Ti–6Al–4V
Density	ρ (kg/m^3)	4428
Shear modulus	G (GPa)	41.9
Poisson's ratio	ν	0.31
J–C yield strength	A (MPa)	1098
J–C hardening coefficient	B (MPa)	1092
J–C strain hardening exponent	N	0.93
J–C strain rate constant	C	0.014
J–C softening exponent	M	1.1
Melting temperature	T_m (K)	1878
J–C damage constant	d_1	−0.09
J–C damage constant	d_2	0.27
J–C damage constant	d_3	0.48
J–C damage constant	d_4	0.014
J–C damage constant	d_5	3.87
Elastic bulk wave velocity	C_0 (km/s)	5.13
Slope in u_s vs. u_p diagram	S	1.028
Grüneisen coefficient	γ_0	1.23
Fracture toughness	K_{IC} (MPa m$^{1/2}$)	49.9–100
Specific heat	c (J/kg °C)	560
Heat fraction	α_0	0.9

various incidence angles (i.e., normal or oblique impact as shown in Fig. 1b). The impact velocity was measured using a Chronograph.

The impact velocities in the present study were 182.88 and 243.84 m/s, and two impact angles of 90° and 45° were used. Under each testing condition, a total of three specimens were tested. The craters formed by impact were characterized using a white-light scanner and an optical microscope. The line profiles extracted from the white-light scanning results were compared against those predicted by the FE models.

3. Modeling approach

3.1. Numerical model

A three-dimensional, numerical model representative of the FOD testing was developed using the explicit finite element code Abaqus/Explicit [14]. The eight-node brick hexahedral elements with one integration point (C3D8R) were used in the simulation. Fig. 2 shows a typical finite element mesh created for the target and the spherical projectile. A refined, uniform mesh was used in the impact region indicated in the figure. Due to the symmetry, only half of the geometry was modeled to save the computational cost. The symmetry planes were constrained not to move in the Z-direction. The movement of the target along Y-direction was constrained by contact from a fully constrained rigid cover sheet and rigid support. Mesh sensitivity analysis was conducted to ensure that the mesh was optimized for stability, accuracy, and efficiency of the impact analysis. In other words, the chosen mesh needs to ensure that the model can provide a convergent solution (i.e., errors of displacement and plastic strains comparing with those from a finer mesh model are less than 5%), predict the experimental measurements, and allow the maximum saving of the computational cost. The results presented in this paper are based on this optimized mesh.

In the simulation, the alumina projectile was modeled as elastic and the steel one as elastic–plastic, with the parameters given in Table 1. A more sophisticated material model was employed for Ti–6Al–4V to simulate the dynamic response and will be discussed next.

3.2. Material models

In impact analysis, the material constitutive law should include strain rate dependency for both material deformation and failure. This study investigates the J–C material model in conjunction with Mie–Gruneisen equation of state (EOS) model to simulate the response of Ti–6Al–4V under FOD impact conditions.

3.2.1. J–C material model

In general, the response of material under high-speed impact conditions/events involves consideration of effects of strain, strain rate, and temperature. The J–C plasticity model [1,12,15] was employed to model the flow stress behavior of ductile materials. The J–C model represents the von Mises flow stress $\overline{\sigma}$ as a function of the equivalent plastic strain $\overline{\varepsilon}^{pl}$, equivalent plastic strain rate $\dot{\overline{\varepsilon}}^{pl}$, and temperature, T as

$$\overline{\sigma} = \left(A + B\left(\overline{\varepsilon}^{pl}\right)^n\right)\left[1 + C\ln\left(\dot{\overline{\varepsilon}}^{pl}/\dot{\overline{\varepsilon}}_0^{pl}\right)\right]\left(1 - T^{*m}\right) \quad (1)$$

where A, B, C, and m are constants; n is strain hardening exponent; $\dot{\overline{\varepsilon}}^{pl}/\dot{\overline{\varepsilon}}_0^{pl}$ is the normalized equivalent plastic strain rate (typically normalized to a plastic strain rate of 1.0 s^{-1}); and T^* is the homologous temperature defined as

$$T^* = (T - T_{room})/(T_{melt} - T_{room}) \quad (2)$$

where T is the material temperature, T_{melt} is the melting temperature, and T_{room} is the room temperature. For high rate deformation problems, it is often assumed that the deformation takes place under adiabatic conditions and an arbitrary percentage of the plastic work done during deformation is converted into heat. For many materials, 90–100% of the plastic work is assumed to be dissipated as heat into the material. Thus, the temperature used in Eq. (1) can be derived from the increase in temperature according to the following expression:

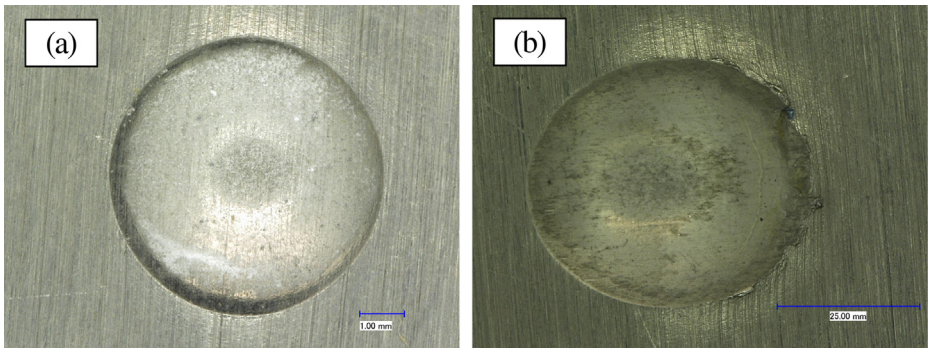

Fig. 3. Impact crater produced by impact of alumina projectile on Ti–6Al–4V for (a) 90° and (b) 45° impact.

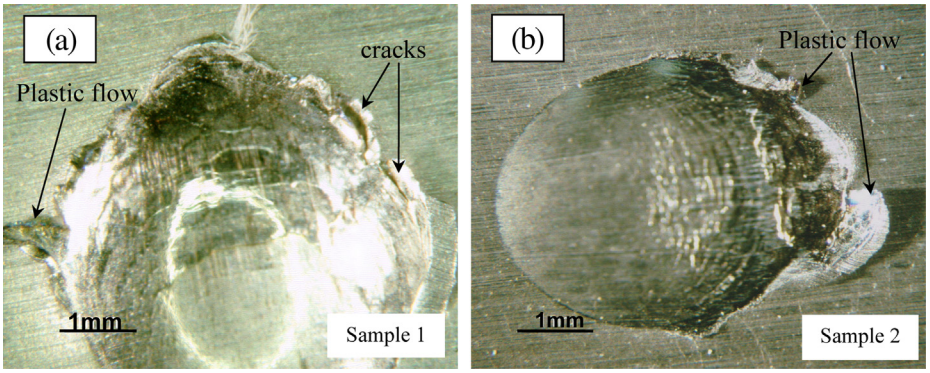

Fig. 4. Impact crater produced by 45° impact of steel projectile on Ti–6Al–4V: (a) sample 1 and (b) sample 2.

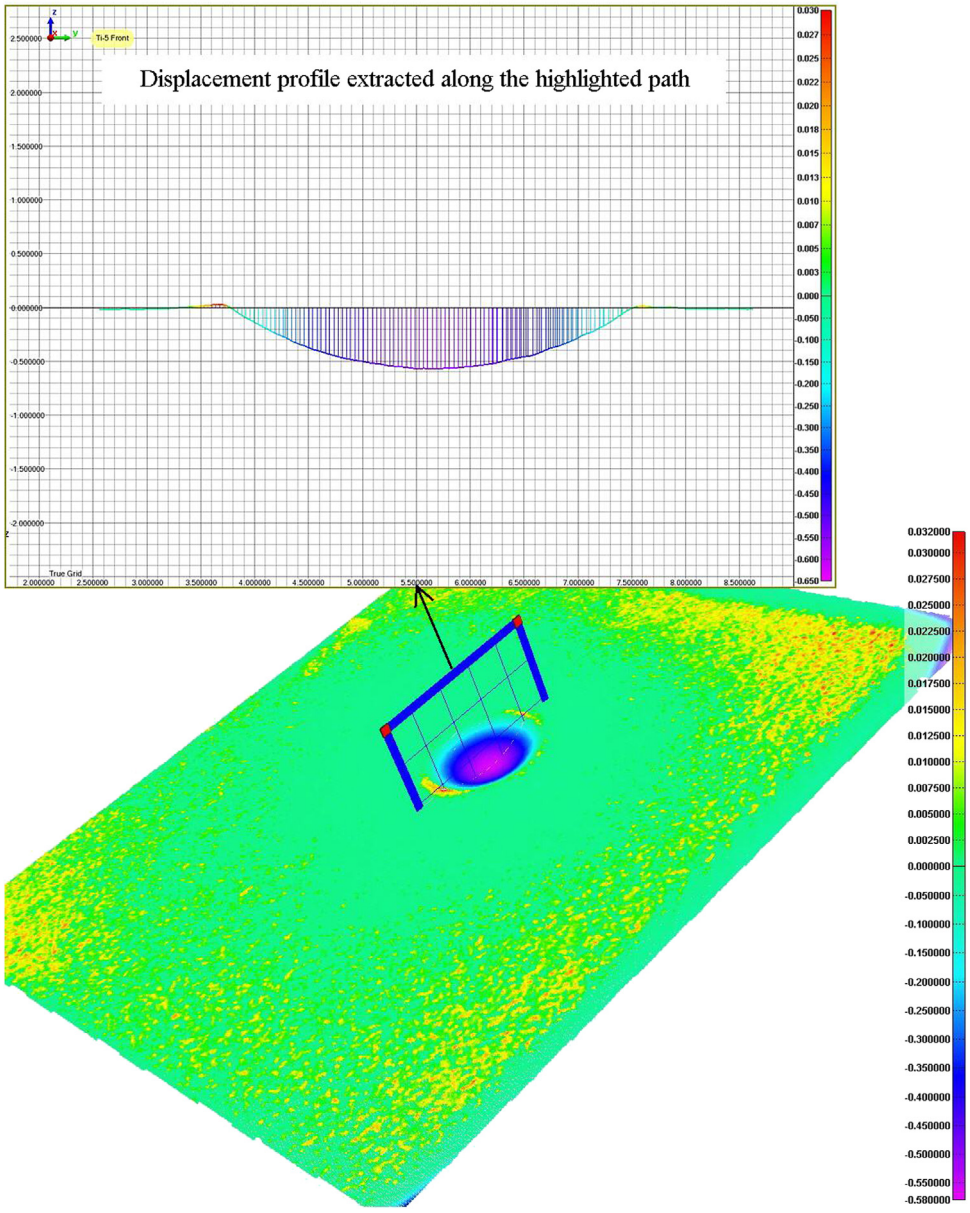

Fig. 5. Post-impact, white-light surface scan for 90° impact of alumina projectile at 243.84 m/s: contour of the out-of-plane displacement and displacement profile extracted along the highlighted path.

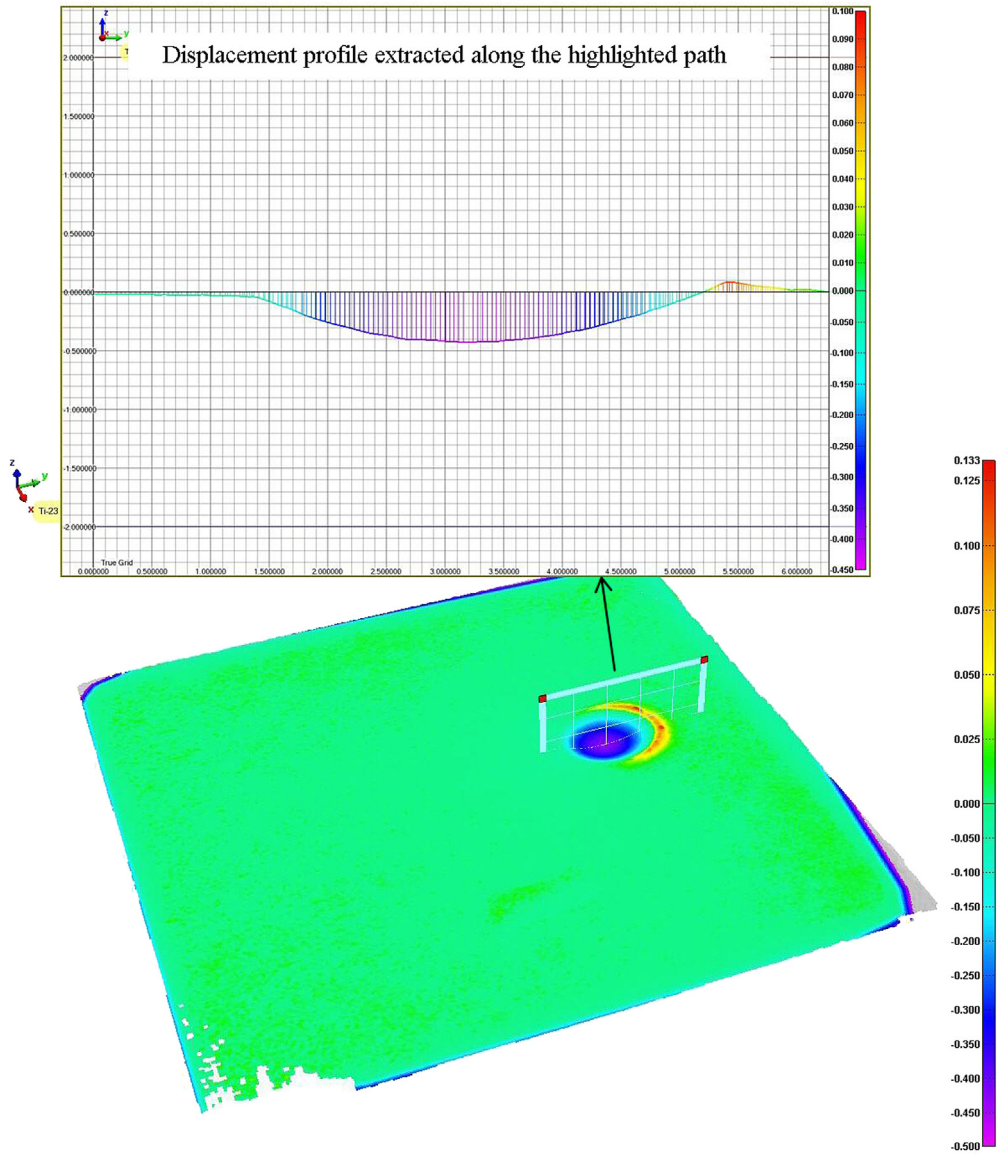

Fig. 6. Post-impact, white-light surface scan for 45° impact of alumina projectile at 243.84 m/s: contour of the out-of-plane displacement and displacement profile extracted along the highlighted path.

$$\Delta T = \alpha_0/\rho c \cdot \int \sigma(\varepsilon)\mathrm{d}\varepsilon \tag{3}$$

where ΔT is the temperature increase, α_0 is the percentage of plastic work transformed to heat, c is the heat capacity, and ρ is the density. In the present simulation, the effect of adiabatic heat was not considered since its influence on the results (e.g., deformation and plastic strain) is less than 1%.

In addition to deformation, damage in the forming voids and shear bands may develop under dynamic loading. This process can be modeled using the J–C progressive damage model. The progressive damage model supports the specification of damage initiation criterion as well as damage evolution. The general expression for the equivalent plastic strain at the onset of damage in the J–C model [1,12,15] is given by:

$$\bar{\varepsilon}_{\mathrm{D}}^{\mathrm{pl}} = [d_1 + d_2\exp(-d_3\eta)]\left[1 + d_4\ln\left(\dot{\bar{\varepsilon}}^{\mathrm{pl}}/\dot{\bar{\varepsilon}}_0\right)\right]\left(1 + d_5 T^*\right) \tag{4}$$

where $\eta = -p/\bar{\sigma}$ is the stress triaxiality defined as the ratio of the pressure, p, to the von Mises stress, $\bar{\sigma}$, and d_1–d_5 are constants. Damage occurs when the damage parameter $D = \sum \Delta\bar{\varepsilon}^{\mathrm{pl}}/\bar{\varepsilon}_{\mathrm{D}}^{\mathrm{pl}}$ reaches a value of 1.0. After damage initiation, the material stiffness is degraded progressively according to the specified damage evolution relationship. A fracture-energy-based progressive damage

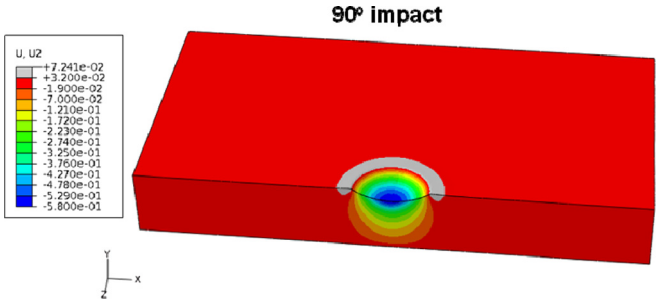

Fig. 7. Contour of vertical displacement (U2) predicted by the FE model for 90° impact at the velocity of 243.84 m/s by alumina projectile.

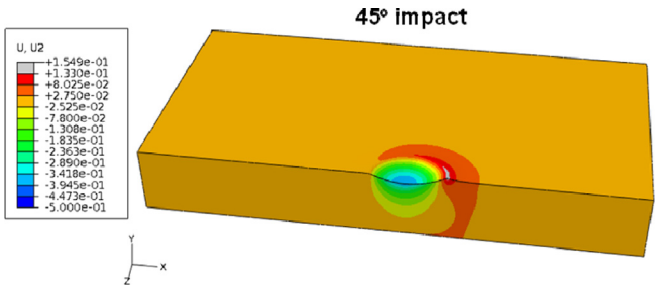

Fig. 8. Contour of vertical displacement (U2) predicted by the FE model for 45° impact at the velocity of 243.84 m/s by alumina projectile.

evolution approach provided by Abaqus/Explicit was used to characterize damage evolution by progressively degrading the material stiffness that finally led to material failure with the overall damage variable D, given below, reaching 1 [14].

$$D = 1 - \exp\left(- \int_0^{\bar{u}^{\mathrm{pl}}} \frac{\bar{\sigma}_y \dot{\bar{u}}^{\mathrm{pl}}}{G_c} \, \mathrm{d}t \right) \tag{5}$$

The formulation of the model ensures that the energy dissipated during the damage evolution process equal to the critical strain energy release rate, G_c. Once the maximum degradation of the element stiffness was reached, the element was deleted and removed from the model.

3.2.2. Mie–Grüneisen EOS

The Mie–Grüneisen EOS [9,16] was employed to simulate the volumetric response of the material under shock regime. The linear shock velocity, u_s, and material particle velocity, u_p, are related by the following equation:

$$u_s = C_0 + S u_p \tag{6}$$

where C_0 is the intercept of the u_s–u_p curve (usually the elastic bulk wave velocity) and S is the coefficient slope of the u_s–u_p curve.

With the above relation, the Mie–Grüneisen EOS model defines pressure for compressed materials as

$$p = \rho_0 C_0^2 \mu \left[1 + (1 - \gamma_0/2)\mu - (a/2)\mu^2\right] \Big/ [1 - (S-1)\mu]^2 + \gamma_0 E_{\mathrm{int}} \tag{7}$$

and for expanded materials as

$$p = \rho_0 C_0^2 \mu + (\gamma_0 + a\mu) E_{\mathrm{int}} \tag{8}$$

where E_{int} is the internal energy, γ_0 is the Grüneisen gamma, a is the first order volume corrections to γ_0, and μ is given as

$$\mu = \rho/\rho_0 - 1 \tag{9}$$

where ρ is the current density and ρ_0 is the initial density.

For Ti–6Al–4V, C_0 is about 5 km/s, while S is approximately one (see Table 2). So the shock velocity is higher than the material velocity by about 5 km/s. The material parameters to define the Mie–Grüneisen EOS and J–C material model are given in Table 2. These parameters were taken from existing literature on Ti–6Al–4V [9,12,15].

4. Results and discussion

4.1. Experimental results

Figs. 3 and 4 present optical photographs of the typical craters created by impact of alumina and steel projectiles on Ti–6Al–4V, respectively. A characteristic crater pattern consisting of a central depression and a peripherical rim of displaced material can be discerned in these figures. Neither the alumina nor the steel projectiles showed any damage or permanent deformation after impact. In the case of alumina projectile impacting Ti–6Al–4V, the crater formation was mainly due to plastic deformation. Thus, the measurements from this set of experiments were used to validate the J–C plasticity model. However, in the case of steel projectile, cracks and material removal were observed near the rim of the crater. Thus, the measurements from this set of experiments were used to validate the J–C damage model.

After the impact experiments, the specimen was scanned using the white-light interferometer to extract the crater shapes and dimensions, which are directly compared against FE model. Figs. 5 and 6 show typical scanning results of the craters formed at the impact velocity of 243.84 m/s by impact of alumina projectiles at the impact angles of 90° and 45°, respectively. The target surface far from the impact site is set as the zero reference. Line profiles can be extracted from the contours to provide direct comparison with the corresponding FE modeling results.

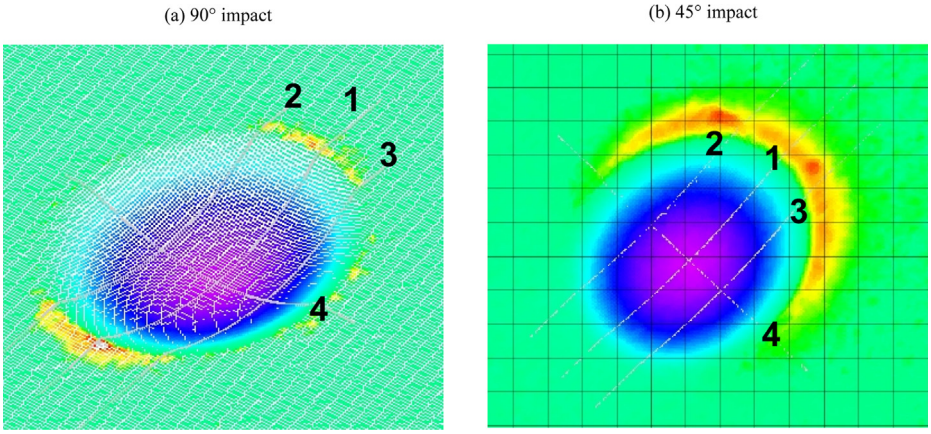

Fig. 9. Illustration of four paths along which displacement profiles were extracted: (a) 90° and (b) 45° impact.

4.2. Numerical predications and correlations with experiments

4.2.1. Validation of the J–C plasticity model

Figs. 7 and 8 show the dent shape predicted by the FE model at the impact velocity of 243.84 m/s and the impact angle of 90° and 45°, respectively. Similar to the experimental measurement, the displacement profile along the specified path was also extracted from the FE results. To directly compare the predicted and measured crater shape, four scanning paths (1–4), as illustrated in Fig. 9, were selected to extract the line profile of the crater. Path 1 is along the center line of the crater. Paths 2 and 3 are approximately mid-way between the center path and the crater rim. Since the model only simulates half of the geometry, the predictions along paths 2 and 3 are technically identical. Path 4 is another center line of the crater and perpendicular to path 1. The FE results are compared against the experimental data for all testing conditions. Figs. 10 and 11 comparably show the measured and predicted profiles extracted along all paths for both 90° and 45° impact at the velocity of 243.84 m/s, respectively. It is clear that the predicted impact crater profiles agree well with those measured from the experiments.

The similar comparisons were also performed for both 90° and 45° impact at a relatively lower velocity of 182.88 m/s. As an example result, only the crater profiles extracted along the center path (path 1) were presented in Fig. 12 for 90° and 45° impact at the velocity of 182.88 m/s. Again, good agreement is observed between experimental measurements and FEA.

From the above comparisons of the deformation shape and crater profile, it can be concluded that the FEA with the J–C plasticity model can predict the localized plastic deformation accurately at various impact velocities and impact angles. Thus, the J–C

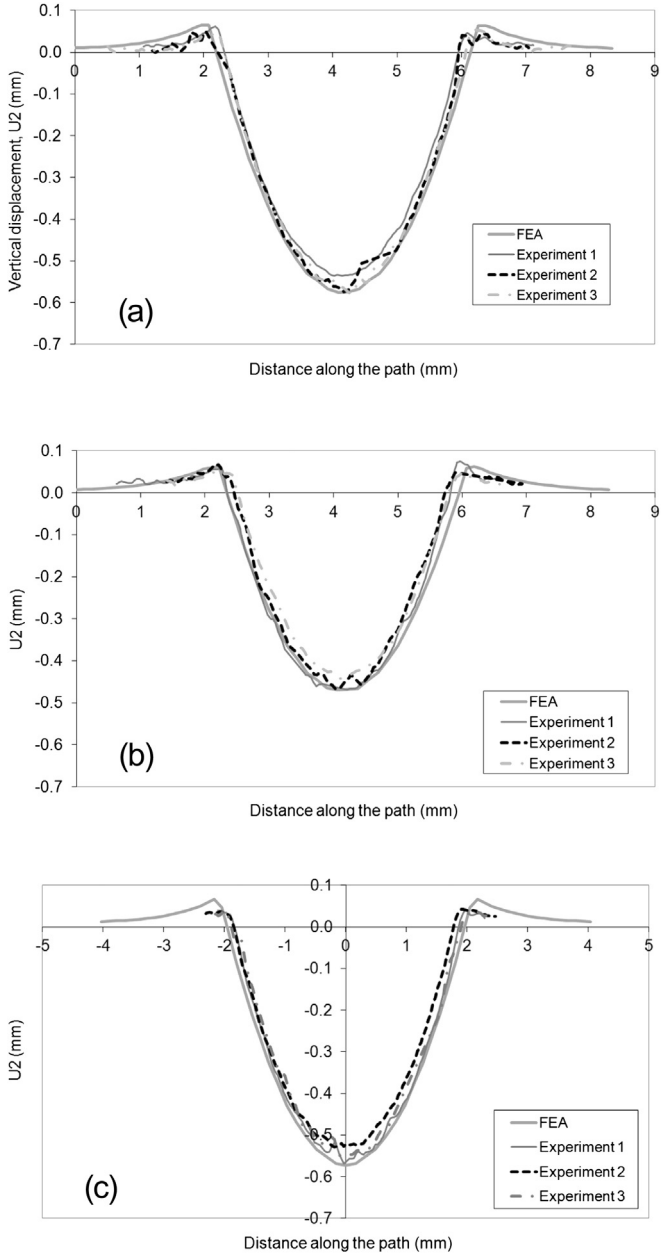

Fig. 10. Comparison of the predicted and measured crater profiles extracted along (a) path 1, (b) path 2/3, and (c) path 4 as illustrated in Fig. 9 for 90° impact at the velocity of 243.84 m/s by alumina projectile.

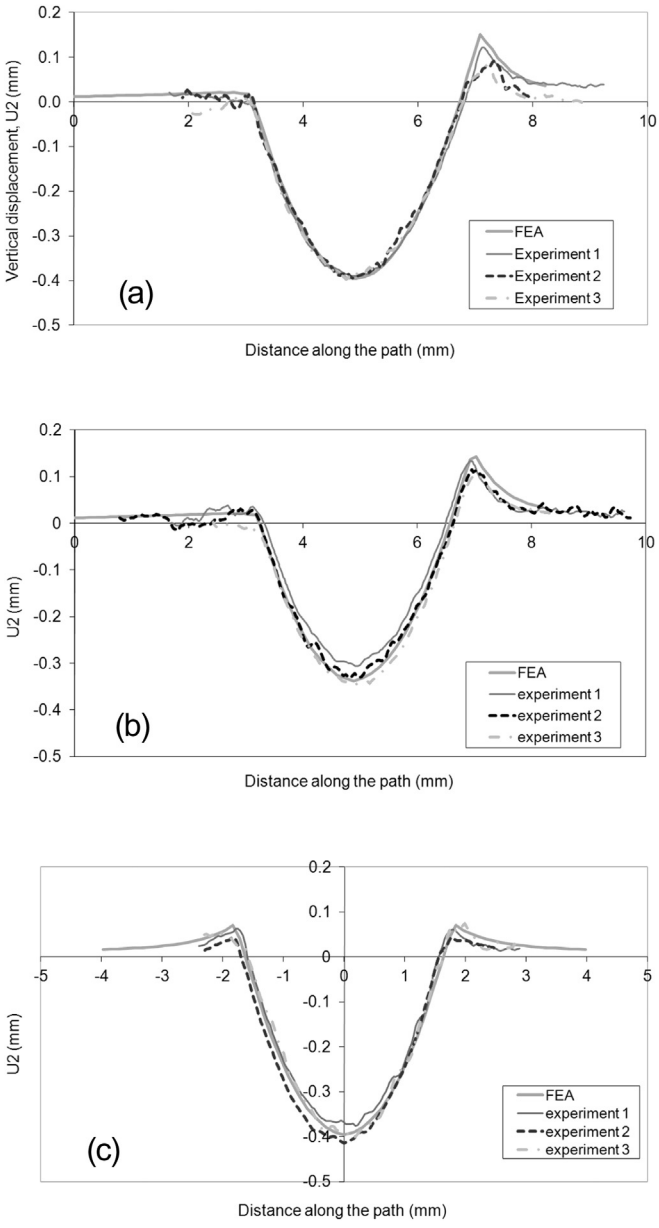

Fig. 11. Comparison of the predicted and measured crater profiles extracted along (a) path 1, (b) path 2/3, and (c) path 4 as illustrated in Fig. 9 for 45° impact at the velocity of 243.84 m/s by alumina projectile.

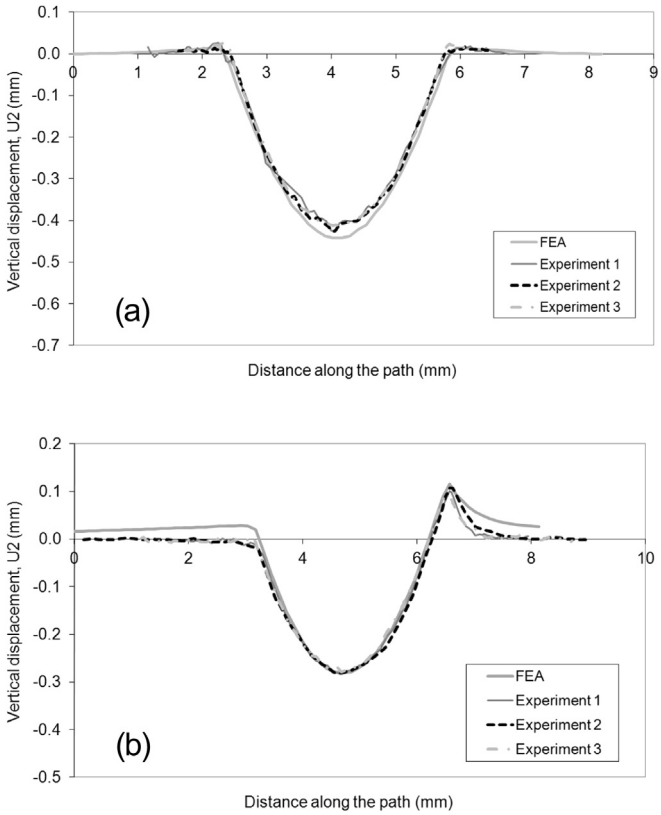

Fig. 12. Comparison of the predicted and measured crater profiles extracted along the center path (path 1) as illustrated in Fig. 9 for (a) 90° and (b) 45° impact at the velocity of 182.88 m/s by alumina projectile.

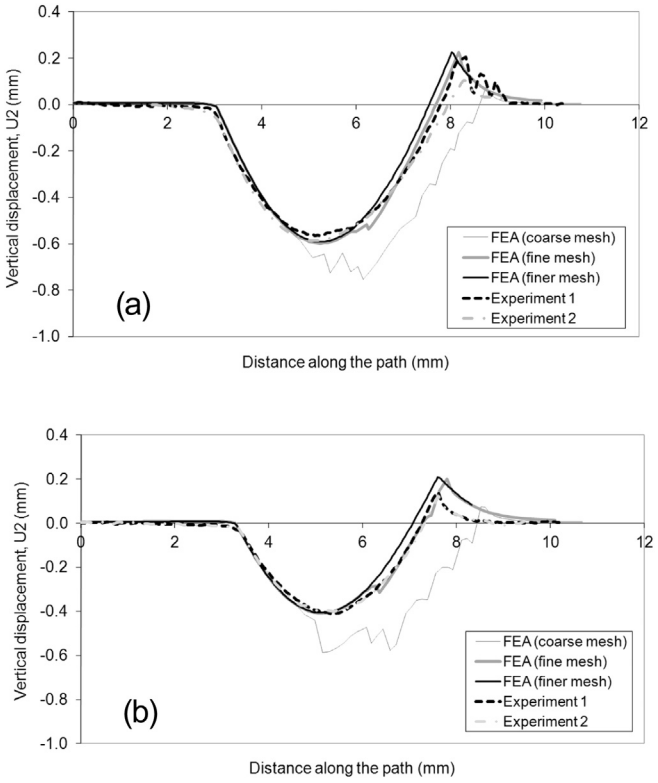

Fig. 13. Comparison of the predicted crater with the experimental measurements at impact velocity = 243.84 m/s by steel projectile: along (a) the center path (path 1) and (b) path 2 as indicated in Fig. 9b.

plasticity model is validated for the present simulation conditions with the strain rates in range of 10^4–10^6 s^{-1}.

4.2.2. Validation of J–C damage model

Damage and failure introduces a strong mesh dependency due to strain localization. Therefore, mesh convergence study was also performed to alleviate the mesh dependency in the simulation of the damage and failure. To save computational cost, the mesh refinement was strictly and uniformly applied in the impact region (as indicated in Fig. 2). Three mesh densities were studied: the coarse mesh has 4800 elements in the impact region, the fine mesh has 30,720 elements, and the finer mesh has 196,608 elements. As a reference, each element of the fine mesh has the size about 0.127 mm × 0.127 mm × 0.129 mm.

Fig. 13a and b compare the predicted craters with the experimental results for 45° impact at the impact velocity of 243.84 m/s. The figures include the results from the models with different mesh densities.

From the above figures it is seen that the results from the coarse mesh model does not agree with the experimental results. The difference is mainly due to the material loss of the target under impact. In the simulation, fully damaged elements were deleted from the crater toward the raised lip. The coarse mesh model predicted relatively more aggressive material loss at the impact site. However, in the fine and finer mesh models, only the top layer elements in the crater close to the raised lip were full damaged and removed from the models. Both results show significant improvement and better agreement with the experimental results. The slight difference between the fine and finer mesh results is contributed by the difference of the element thicknesses. Since the error is less than 5%, it can be concluded that the results have converged to the experimental results with the increase of the mesh density. It can be also concluded that good agreements with the experimental results indicate positively validation of the J–C failure model with fracture-energy-based damage evolution for the FOD simulation.

5. Conclusion

In the present paper, FOD experiments and simulations were performed to investigate the dynamic response and the material modeling of Ti–6Al–4V at impact strain rates of the order of 10^4–10^6 s^{-1}. Excellent agreements between the experimental measurements and numerical predictions are demonstrated in all cases considered. The numerical model is validated for the present application. The validation of the J–C plasticity and damage model provides the basis for using this material model in simulation of other dynamic problems such as sand erosion behavior of Ti–6Al–4V.

Acknowledgements

This project was funded by the Vertical Lift Consortium (VLC), formerly the Center for Rotorcraft Innovation and the National Rotorcraft Technology Center (NRTC), U.S. Army Aviation and Missile Research, Development and Engineering Center (AMRDEC) under Technology Investment Agreement W911W6-06-2-0002, entitled National Rotorcraft Technology Center Research Program. The authors would like to acknowledge that this research and development was accomplished with the support and guidance of the NRTC and VLC. The views and conclusions contained in this document are those of the authors and should not be interpreted as representing the official policies, either

expressed or implied, of the AMRDEC or the U.S. Government. The U.S. Government is authorized to reproduce and distribute reprints for Government purposes notwithstanding any copyright notation thereon.

References

[1] Johnson GR, Cook W. Fracture characteristics of three metals subjected to various strains, strain rates, temperatures and pressures. Eng Fract Mech 1985;21(1):31–48.

[2] Macdougall DAS, Harding J. A constitutive relation and failure criterion for Ti6Al4V alloy at impact rates of strain. J Mech Phys Solids 1999;47:1157–85.

[3] Meyer Jr HW, Kleponis DS. Modeling the high strain rate behavior of titanium undergoing ballistic impact and penetration. Int J Impact Eng 2001;26:509–21.

[4] Tham CY, Tan VBC, Lee HP. Ballistic impact of a KEVLAR® helmet: experiment and simulations. Int J Impact Eng 2008;35:304–18.

[5] Peirs J, Verleysen P, Van Paepegem W, Degrieck J. Determining the stress–strain behaviour at large strains from high strain rate tensile and shear experiments. Int J Impact Eng 2011;38:406–15.

[6] Kalumuck KM, Chahine GL, Haynie DA. Helicopter blade leading edge protection study. In: Field JE, Dear JP, editors. Proceeding of seventh international conference on erosion by liquid and solid impact. Cambridge, UK: Cavendish Laboratory; 1987.

[7] Barkoula N-M, Karger-Kocsis J. Review processes and influencing parameters of the solid particle erosion of polymers and their composites. J Mater Sci 2002;37:3807–20.

[8] ElTobgy MS, Ng E, Elbestawi MA. Finite element modeling of erosive wear. Int J Mach Tool Manuf 2005;45:1337–46.

[9] Wang Y, Yang Z. Finite element model of erosive wear on ductile and brittle materials. Wear 2008;265:871–8.

[10] Wang X, Shi J, El-Wardany T, Kumar RS, Bagai A. Numerical prediction of sand erosion for helicopter blade erosion protection. 67th American Helicopter Society international annual forum 2011, Virginia Beach, Virginia; June 2011.

[11] Duó P, Liu J, Dini D, Golshan M, Korsunsky AM. Evaluation and analysis of residual stresses due to foreign object damage. Mech Mater 2007;39:199–211.

[12] Lesuer DR. Experimental investigations of material models for Ti–6Al–4V titanium and 2024-T3 aluminum. FAA report, DOT/FAA/AR-00/25 September 2000.

[13] Khan AS, Suh YS, Kazmi R. Quasi-static and dynamic loading response and constitutive modeling of titanium alloys. Int J Plasticity 2004;20:2233–48.

[14] Abaqus analysis user's manual, version 6.10; 2010.

[15] Kay G. Failure modeling of titanium Ti–6Al–4V and aluminum 2024-T3 with the Johnson–Cook material model. FAA report, DOT/FAA/AR-03/57 September 2003.

[16] Loikkanen MJ, Buyuk M, Kan CD, Meng N, A computational and experimental analysis of ballistic impact to sheet metal aircraft structures. in: Proceedings of the 5th European LS-DYNA users conference, Bimingham, UK; May 2005.